Kinematic artifacts in the subsurface-offset extended image and their elimination by a dip-domain specularity filter

Raanan Dafni[1] and William W. Symes[1]

ABSTRACT

Common-image gathers in the dip-angle domain may be computed in relation to wave-equation migration methods, extended by the subsurface offset. They involve the application of a postmigration local Radon transform on the subsurface-offset extended image. In the dip-angle domain, seismic reflections are focused around the specular dip angle of reflection. This focusing distinguishes them from any other event in the image space. We have incorporated the dip-angle information about the presence of specular reflections into the computation of the conventional scattering-angle-dependent reflection coefficient. We have designed a specularity filter in the dip-angle domain based on a local semblance formula that recognizes and passes events associated with specular reflections, while suppressing other sorts of nonspecular signal. The filter is remarkably effective at eliminating either random or coherent noises that contaminates the prestack image. In particular, our dip-angle filter provides a method for the suppression of kinematic artifacts, commonly generated by migration in the subsurface-offset domain. These artifacts are due to an abrupt truncation of the data acquisition geometry on the recording surface. We have studied their appearance and devised an appropriate formation mechanism in the subsurface-offset and scattering-angle domains. The prominent presence of the kinematic artifacts in image gathers usually impairs the quality of the postmigration analysis and decelerates the convergence of wave-equation inversion techniques. We have determined from testing on synthetic and field data that using the proposed dip-angle-domain specularity filter efficiently eliminates the kinematic artifacts in the delivered gathers. We expect involvement of the specularity filter to increase the reliability and quality of the seismic processing chain and provide a faster convergence of iterative methods for seismic inversion.

INTRODUCTION

Wave-equation prestack depth migration (PSDM) algorithms use a downward continuation of the wavefield through the complexity of the subsurface model. Unlike Kirchhoff migration methods, no high-frequency asymptotic assumptions associated with the ray theory are required. In areas where the subsurface geology is complicated and strong lateral velocity variations exist, these asymptotic methods may contaminate the image with noise and artifacts (Červený, 2001; Gray et al., 2001). Therefore, wave-equation migration methods are particularly preferred for imaging in structurally complex regions. However, wave-equation methods usually require a significant amount of computational resources. Tremendous advances in software and hardware technology achieved in the past two decades alleviate some of these technical difficulties.

Migration velocity analysis and amplitude variation analysis use prestack common-image gathers (CIGs), computed as a part of seismic imaging. The artifacts associated with Kirchhoff migration and its asymptotic assumptions reappear in the computation of prestack CIGs, and might induce severe errors in the analysis and increase the discrepancy with the real subsurface model (Baina et al., 2006; Moser, 2011). Choosing wave-equation migration methods over Kirchhoff methods for the CIGs computation enhances the reliability and accuracy of the prestack information. The increasing interest in wave-equation inversion techniques, such as full-waveform inversion (FWI), is another evolutionary evidence for the importance of wave-equation-based methods. Exploiting the redundancy of the seismic data to invert for the medium parameters necessitates the extension of the reflectivity by an additional axis, or in other words by computing CIGs (Symes, 2008; Stolk et al., 2009).

The horizontal subsurface offset, as introduced by Claerbout (1985) in the framework of survey-sinking migration, is a common and natural extension for wave-based imaging methods. It is defined as the horizontal offset vector connecting the sunken shot and receiver in the subsurface and involves an action at a distance between the incident and scattered wavefields. The subsurface offset parameterizes the reflectivity in the image space, rather than in the recorded data space, after focusing at the reflection point. However, it lacks a physical meaning because applying stress at one point cannot cause strain at a distance. Elastic material under stress develops strain only at the exact location of interaction. Hence, finite subsurface offsets are considered as nonphysical offsets. A perfectly focused image at the zero subsurface offset (the physical offset) is expected when the exact velocity model is used. A common difficulty that usually arises in computing subsurface-offset CIGs is the appearance of kinematic artifacts away from the zero-offset trace (Mulder, 2014). Like other coherent noise, these artifacts can impede velocity model optimization and their elimination might become a real challenge.

The local angle domain has been proposed and promoted as the most intuitive extension of the reflectivity (Bleistein, 1987; Miller et al., 1987; Xu et al., 2001; Koren and Ravve, 2011; Ravve and Koren, 2011; ten Kroode, 2012). Decomposing the angle-dependent reflection coefficients as angle-domain CIGs (ADCIGs) is directly related to the medium parameters and has a clear physical mechanism. The angle domain has been studied extensively over the years. The analysis of ADCIGs can ease imaging tasks over complex geology by unfolding multivalued raypaths (Prucha et al., 1999). Two independent angular systems are intrinsically involved: the scattering-angle and the dip-angle system. The first one provides Snell's law-related information according to the scattering angle at the local reflecting surface, and the latter exposes information about the orientation of the reflecting surface (the specular direction). Although scattering-angle ADCIGs are widely used and studied, dip-angle ADCIGs gain some attention as well in recent years. However, in most of the published studies, the dip domain is considered as an attribute of Kirchhoff migration methods. It was found as an attractive domain for using structural-based algorithms to reduce Kirchhoff imaging artifacts (Audebert et al., 2003; Baina et al., 2003; Chen, 2004; Bienati et al., 2009). Incorporating dip-domain information in decomposing the scattering-angle ADCIGs has been revealed as beneficial in terms of the efficiency and accuracy of the postmigration analysis (Koren and Ravve, 2011; Dafni and Reshef, 2014). Furthermore, the dip domain also enables the separation of seismic diffractions from reflections according to their distinguished response (Landa et al., 2008; Koren and Ravve, 2010; Klokov and Fomel, 2012). The analysis of seismic diffractions in the dip domain increases the image resolution with regard to small-scale geologic objects, such as faults and fractures (Landa and Keydar, 1998; Khaidukov et al., 2004), and it has high sensitivity to migration velocity errors (Fomel et al., 2007; Reshef and Landa, 2009; Reshef et al., 2011).

Dafni and Symes (2016) propose a suite of Radon transform operators to transform subsurface-offset CIGs to ADCIGs derived from wave-equation migration. The operators were described as image space constructions, applied after the migration of the seismic data. Two angle axes, representing scattering-angle ADCIG and dip-angle ADCIG, were derived from a unidimensional subsurface-offset extension. The corresponding inverse operators, trans-

forming the ADCIGs back to the subsurface-offset domain, were formulated as well. These allow the prestack image to be analyzed in both domains, back and forth, by simple postmigration transformations.

In this study, we follow Dafni and Symes's (2016) angle-domain decomposition techniques and demonstrate the relationship between wave-equation migration methods and the dip-angle domain. The beneficial information provided by dip-angle ADCIGs is not restricted only to Kirchhoff-migration methods anymore. A specularity filter is designed in the dip domain to suppress noise and nonspecular contributions to the image. We apply this filter to synthetic and field data examples and show its efficacy in improving image quality and reliability. Because the subsurface offset constitutes a starting point for the angle domain in this study, special attention is given to the elimination of the kinematic artifacts in the subsurface-offset domain by the specularity filter. First, we describe the formation mechanism of these artifacts and its transform to the scattering-angle domain. Then, a successful elimination is executed by the suggested filter in the dip-angle domain. Moreover, the proposed specularity filter is also shown as highly effective in the case when the velocity model is unknown. Because this is a structural-based filter, it efficiently preserves only the essential moveout information needed for accurate migration velocity analysis or for the convergence of wave-equation inversion methods.

KINEMATIC ARTIFACTS IN THE SUBSURFACE-OFFSET DOMAIN

The wave-equation prestack migration operator is extended to the subsurface-offset domain by taking the adjoint of a Born-type modeling operator, after extending the definition of the reflectivity to depend on the extra degree of freedom (Symes, 2008). The reflectivity $I(\mathbf{x}, \mathbf{h})$, extended by the subsurface half-offset $\mathbf{h}$, is formulated as

$$I(\mathbf{x}, \mathbf{h}) = \int d\mathbf{x_r} \int d\mathbf{x_s} \int dt \frac{\partial^2}{\partial t^2} D(\mathbf{x_r}, t; \mathbf{x_s})$$
$$\times \int d\tau G(\mathbf{x} + \mathbf{h}, t - \tau; \mathbf{x_r}) G(\mathbf{x} - \mathbf{h}, \tau; \mathbf{x_s}), \quad (1)$$

where $G(\mathbf{x}, t)$ is the Green's function, $D(\mathbf{x_r}, t; \mathbf{x_s})$ stands for the seismic data, and τ is the migration time. In this work, we implemented our migration operator according to equation 1, by restricting the offset extension to the horizontal direction solely. We also restrict our attention to two dimensions. Three dimensions work the same way, but for reasons of computational economy, only 2D examples will be presented here. Thus, the subsurface half-offset is a scalar from now on.

The image is expected to focus at the physical zero subsurface offset, when the correct velocity model is used. However, this focusing is often observed as incomplete when some signal "leaks" to nonzero subsurface offsets. This leakage is demonstrated next via a simple two-layer synthetic model, consisting of a −5° dipping reflection interface and known velocity model. The synthetic data were simulated by an acoustic Born modeling operator, which solves the perturbational wave equation by a fourth order in space and second order in time finite-difference extrapolator. Trace data were computed for 161 shots across the model with 50 m spacing. The 401 receivers were evenly spread in front and behind each shot with 25 m spacing (split-spread geometry). A Ricker wavelet with

8 Hz dominant frequency was used as a source. For imaging, we used the extended Born-type migration operator in equation 1. The subsurface-offset extension was sampled with 25 m grid spacing up to a maximum of 2500 m. Figure 1 shows the subsurface-offset extended image. Three image sections are displayed in Figure 1a. The middle one is the zero subsurface offset image section, whereas the top and bottom sections correspond to nonzero subsurface offsets ($h = -300$ and 300 m, respectively). A single subsurface-offset CIG, calculated at $x = 10,000$ m, is also shown in Figure 1b. The offset traces, representing the image sections in Figure 1a, are marked with the black arrows on the gather. A weak but considerable signal is clearly leaking and contaminating the nonzero offsets with kinematic artifacts. They are coherent and give a false image of the reflector. Regarding the image phase space, an amplitude polarity reversal is observed above and below the true depth of the reflector.

Mulder (2014) describes the relationship between these artifacts and the acquisition geometry. According to his thesis, they occur as an edge effect due to the abrupt truncation of the acquisition pattern by a maximum offset. In the following, we analyze this phenomenon from a different perspective. We treat prestack migration as a superposition of subsurface-offset extended impulse responses, made by individual data traces. In their paper, Dafni and Symes (2016) derive an elliptic expression for the migration response of a single data trace in the subsurface-offset domain. They assume a delta-function seismic event recorded at the time t_{sr}, and a homogeneous medium with constant velocity V. For a given data trace, acquired at the midpoint x_m by the acquisition half-offset H, the extended impulse response takes the form

$$\frac{(x - x_m)^2}{\left(\frac{1}{2} V t_{sr}\right)^2} + \frac{z^2}{\left(\frac{1}{2} V t_{sr}\right)^2 - (h - H)^2} = 1. \tag{2}$$

We rewrite this equation according to the travel-time hyperbolic relation to the acquisition offset, and while taking into account migration velocity errors,

$$\frac{(x - x_m)^2}{\varepsilon^2 (z_0^2 + H^2)} + \frac{z^2}{\varepsilon^2 (z_0^2 + H^2) - (h - H)^2} = 1, \tag{3}$$

where z_0 is the zero-dip imaging depth of the seismic event and ε is the ratio between the migration velocity and the true velocity.

Prestack migration in the subsurface-offset domain accumulates the response of the data traces in a trace-by-trace manner, according to equation 3. When the true velocity is known, in-phase constructive interference forms the image of the reflector at the zero-subsurface offset, and out-of-phase destructive interference takes place elsewhere. However, because the acquisition geometry is naturally bounded by a maximum offset, this destructive interference is incomplete. Some nondestructive part is left in the image and forms the kinematic artifacts mentioned above.

The extended impulse response of the data traces recorded at the edges of the acquisition pattern (e.g., maximum offset traces) is the source of these artifacts. Figure 2 simulates the migration of the $-5°$ dipping reflector data with the true migration velocity. It shows a superposition of elliptic impulse responses, calculated by equation 3 after setting $\varepsilon = 1$. The elliptic curves correspond to the data traces acquired by the offsets $H = \pm2500$ m. These are the most-positive and most-negative offset values used to calculate the data in this example. Three image sections are presented in Figure 2 in the same manner as in Figure 1a: The $h = 0$ m image section is displayed in the middle, and the $h = \pm300$ m image sections are shown above and below. The bold black line indicates the true depth of the reflector. As expected, all data trace responses are in-phase, tangent to the reflector position at zero subsurface offset (the middle section). However, when the subsurface offset is finite (top and bottom sections), the nondestructive response of the maximum acquisition offset traces generates an image of a fake reflector (i.e., the kinematic artifacts). It is formed tangent to the ellipses as denoted by the dashed red lines, and perfectly follows the images in Figure 1a. Notice the symmetry between the most-positive and most-negative acquisition offsets (green and blue ellipses, respectively). They change roles when the subsurface offset changes its sign.

The geometry of the kinematic artifacts in the subsurface-offset extended image strongly depends on the acquisition pattern. In our example, the data were acquired with a split-spread geometry. Therefore, the illumination coverage is identical for all image locations. It dictates that the fake reflector, observed away from the zero subsurface offset in Figure 1a, will dip with an angle that slightly differs from the dipping angle of the true reflector. However, the artifacts will show a completely different geometry if the acquisition
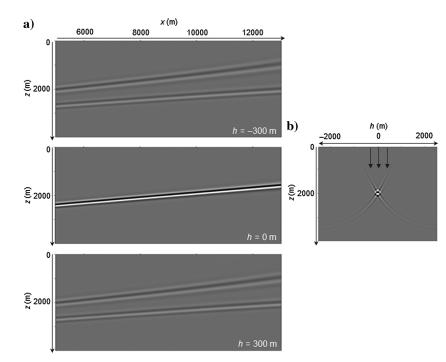

Figure 1. Imaging of a $-5°$ dipping reflector (split-spread acquisition geometry). (a) Three subsurface-offset image sections were extracted from the extended image at $h = -300$, 0, and 300 m (from top to bottom, respectively). (b) Subsurface-offset CIG, calculated at $x = 10,000$ m.

configuration is changed. We demonstrate this by reacquiring the synthetic data for this example with a fixed-spread acquisition geometry in which the receivers are kept stationary on the surface. We migrate the data with the same extended Born-type migration operator. The subsurface-offset extended image is presented in Figure 3 in the same manner as in Figure 1. We obviously recognize that the geometry of the kinematic artifacts has changed. The fake reflectors in the top and bottom panels in Figure 3a are now dipping with an angle that considerably deviates from the dip angle of the true reflector in the middle panel. This is due to a varying illumination coverage across the seismic line. The acquisition geometry truncates differently (i.e., the minimum and maximum offsets) for different image locations, what dictates the place where the artifacts are formed.

We follow the same data truncation formation mechanism to explain the appearance of the kinematic artifacts in the image gather domain as well (i.e., subsurface offset and scattering angle). It is extended here to also deal with the case when velocity errors are present. We separate the discussion between the cases of using true or false migration velocity.

The use of true migration velocity

The extended impulse response represents an elliptic curve in the subsurface-offset domain, after projecting equation 3 on the z-h plane (Dafni and Symes, 2016). It yields

$$\frac{(h - H)^2}{\varepsilon^2(z_0^2 + H^2)} + \frac{z^2}{\varepsilon^2(z_0^2 + H^2) - \Delta x^2} = 1, \qquad (4)$$

where $\Delta x = x - x_m$ is the imaging aperture (image point to midpoint distance). This aperture represents the focal distance of the elliptic response in the gather domain. In addition, note that the ellipse is shifted on the gather axis by the acquisition offset H.

The subsurface-offset CIG in Figure 1b represents the true migration velocity case. Its formation is explained by the top illustration in Figure 4. Elliptic curves, calculated according to equation 4 after setting $\varepsilon = 1$, are accumulated in the figure. The offset H of the data traces, dictates the position of each ellipse in the gather. The image of the reflector is focused constructively at the zero subsurface offset trace, in which all the ellipses intersect. The image is destructively cancelled elsewhere, with the exception involving the response of the most-positive and most-negative acquisition offsets ($H = \pm 2500$ m). The illustration at the bottom of Figure 4 shows these exceptional nondestructive ellipses. It perfectly matches the signal leaking of the kinematic artifacts observed in Figure 1b.

Transformation to the angle domain is achieved by the Radon transform operator proposed by Dafni and Symes (2016). Scattering-angle ADCIGs are computed from the subsurface-offset extended image accordingly. The top of Figure 5 presents the scattering-angle ADCIG computed from the subsurface-offset CIG in Figure 1b. A flat event is shown, indicating the correctness of the migration velocity. We use the same perspective that considers prestack migration as a superposition of extended impulse responses to describe the formation of the image in the angle domain. The elliptic subsurface-offset response from equation 4 is transformed into an angle-domain hyperbolic response. We provide a derivation in Appendix A that describes how ellipses turn into hyperbolas via a parametric Radon transformation. In the scattering-angle domain, the transformed extended impulse response takes the hyperbolic form

Figure 2. Analytic simulation of the $-5°$ dipping reflector's migration. The elliptic impulse responses, contributed by the most-positive and most-negative acquisition offset traces, are accumulated to generate the reflector's image at three subsurface-offset sections: $h = -300$, 0, and 300 m, from top to bottom, respectively.

$$z = \sqrt{(\varepsilon^2(z_0^2 + H^2) - \Delta x^2)(1 + p^2\eta^2)} + pH, \quad (5)$$

$$\eta = \sqrt{\frac{\varepsilon^2(z_0^2 + H^2)}{\varepsilon^2(z_0^2 + H^2) - \Delta x^2}}. \quad (6)$$
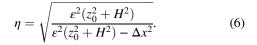
where $p = \tan \gamma$ is the transform's slope and γ stands for the scattering angle. The stretch factor η is derived in Appendix A as well. It expresses the ratio between the semimajor and semiminor axes of the ellipse from equation 4:

The illustration in the middle of Figure 5 demonstrates the transformed superposition of the extended impulse responses in the angle domain. It is calculated according to equation 5 after setting

Figure 3. Imaging of a $-5°$ dipping reflector (fixed-spread acquisition geometry). (a) Three subsurface-offset image sections were extracted from the extended image at $h = -300$, 0, and 300 m (from top to bottom, respectively). (b) Subsurface-offset CIG, calculated at $x = 10{,}000$ m.
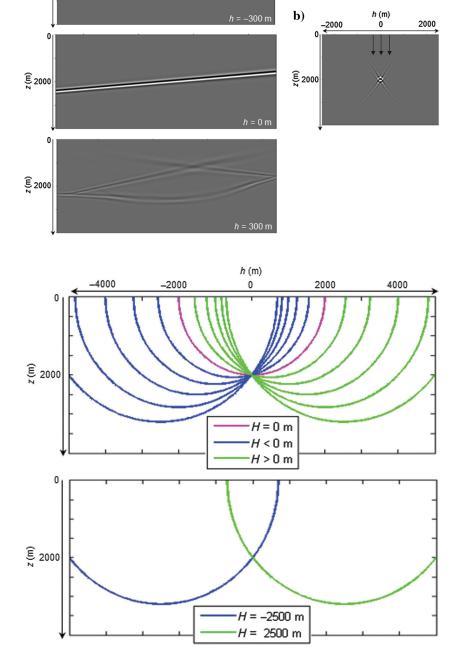

Figure 4. Analytic simulation of the $-5°$ dipping reflector's migration in the subsurface-offset domain. Elliptic impulse responses are accumulated to constructively form the focused reflection event at zero subsurface offset.

$\varepsilon = 1$ to represent the true velocity case. The envelope of all hyperbolas forms the flat event at the reflector's imaging depth of 2000 m (marked with the dotted black line). With regard to the kinematic artifacts in the angle domain, the same formation mechanism is followed. The artifacts are contributed as nondestructive hyperbolic curves by the most positive and most negative acquisition offsets ($H = \pm 2500$ m in our example). At the bottom of Figure 5, these curves are shown individually. They match our observation in the image gather at the top of this figure.
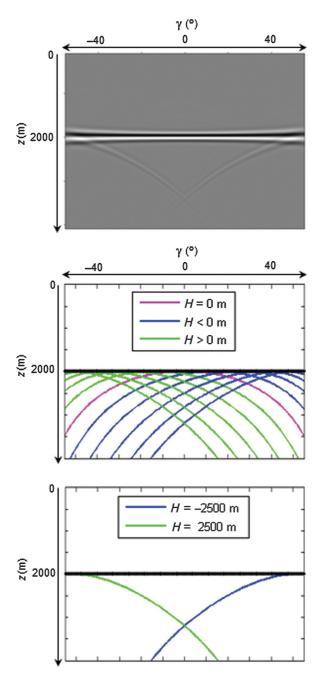

Figure 5. Transformation to the scattering-angle domain. A scattering-angle ADCIG is computed on top, at $x = 10,000$ m. The illustrations below demonstrate the accumulation of the extended impulse responses in the angle domain. A flat event is formed by the envelope of all the hyperbolic curves.

By differentiating equation 5 with respect to the slope p and setting it to zero, we derive an expression for the maximum angle of illumination $p_{\max}$:

$$\pm p_{\max} = \pm \tan \gamma_{\max} = \frac{1}{\eta} \frac{\mp H_{\max}}{\sqrt{\varepsilon^2 (z_0^2 + H_{\max}^2) - H_{\max}^2}}. \quad (7)$$

We find that $p_{\max}$ defines the apex of the kinematic artifacts, and it is directly related to the maximum offset of acquisition $H_{\max}$. Notice that in the special case where a zero-dip reflector is imaged by the true migration velocity ($\varepsilon = 1$), the stretch factor vanishes ($\eta = 1$). In such case, the maximum angle is determined by the simple maximum offset to imaging depth ratio: $\pm p_{\max} = \mp H_{\max} / z_0$.

The hyperbolic angle-domain kinematic artifacts have a reversed amplitude polarization with respect to the flat reflection event. It resembles the classical diffraction curve associated with seismic diffractions (Trorey, 1970), and it is explained here as an angle-domain diffraction curve due to the sharp truncation of the illumination coverage by a maximum angle.

The use of erroneous migration velocity

Imaging with an incorrect migration velocity defocuses the resulting image in the subsurface-offset domain. We demonstrate this by the CIGs at the top of Figure 6a and 6b. The CIGs were calculated by using 10% too-high and too-low migration velocities, respectively. The defocusing of the image is simulated according to equation 4 as a superposition of wrongly migrated elliptic impulse responses, after setting ε to account for the velocity error. It is illustrated in the middle of Figure 6a and 6b by setting ε to 1.1 and 0.9, respectively. The key element in these illustrations is that when velocity is wrong, the ellipses do not share a common intersection point at zero subsurface offset. The defocusing is formed by the envelope of all elliptic curves. It has a curved shape, facing up or down depending on the velocity error. The dotted black line represents this envelope. It was calculated according to the velocity error curve suggested by Bartana et al. (2006). The data truncation kinematic artifacts are deformed in the image gather due to the velocity error, as shown at the bottom of Figure 6a and 6b, where only the nondestructive ellipses are displayed.

In the angle domain, the scattering-angle ADCIGs show moveout curves when velocity errors are present. The image is curving down or up in Figure 7a and 7b, due to the 10% too-high and too-low migration velocities, respectively. Similar to the true velocity case, these moveout curves are formed by the envelope of all hyperbolic responses. This is illustrated in the middle of Figure 7a and 7b by using equation 5, after setting ε to account for the velocity error. The constructive envelope is represented once again analytically by the dotted black line according to Bartana et al. (2006). The hyperbolic imprint of the kinematic artifacts is also illustrated at the bottom of Figure 7a and 7b. The correlation between these illustrations and the scattering-angle ADCIGs at the top of the figure is clearly recognized.

DIP-ANGLE DECOMPOSITION BASED ON SUBSURFACE-OFFSET EXTENDED IMAGING

The decomposition of dip-angle ADCIGs in relation to wave-equation migration is proposed by Dafni and Symes (2016). Forward and inverse local Radon transform operators were formulated

to transform the subsurface-offset extended image to the dip domain and back. The dip-angle response of seismic reflections was revealed in these gathers. It was described as a spot-like response indicating the specular dip angle of the reflection, rather than the familiar concave shape usually produced by Kirchhoff-migration methods. The resolution in dip of the spot-like response is determined by the frequency bandwidth and the velocity function. It is also dictated by the curvature of the imaged events and the effective horizontal range of the local Radon transform.

The dip-angle transformation involves an intermediate stage, in which dip-angle ADCIGs are computed for each individual subsurface offset. The full transformation is complete only after a weighted averaging over all subsurface offsets, according to the weight function W_h (see equations 22–24 in Dafni and Symes, 2016). In this study, we use a normalized Gaussian shaped weight function designed to peak at zero subsurface offset:

$$W_h = \frac{dh}{\sqrt{2\pi\sigma^2}} \exp\left(\frac{-h^2}{2\sigma^2}\right). \tag{8}$$

The Gaussian distribution variance σ^2 is determined heuristically, and it strongly depends on the migration velocity accuracy. The more reliable the velocity is, the less we expect the image to defocus in the subsurface offset, and the smaller the variance. Figure 8a presents the dip-angle ADCIGs, computed in relation to the $-5°$ dipping reflector example mentioned in the previous section. At the top of the figure, the intermediate subsurface offset-dependent dip-angle ADCIGs are shown. They correspond to the subsurface offsets $h = -300$, 0, and 300 m (left to right, respectively). Notice that only the middle gather shows a prominent event at the correct depth-dip position. The two gathers on the sides show the fake dip-domain imprint of the kinematic artifacts. At the bottom of the figure, the final dip-angle ADCIG is computed by averaging the dip-angle contribution of all subsurface offsets, according to the weight function W_h, plotted below. Because the correct migration velocity was used here, we were able to choose a relatively small variance value ($\sigma = 50$ m) in the design of W_h. A well-focused spot is recognized in the resulting dip-angle ADCIG at the true depth of reflection. It indicates the $-5°$ specular dip-angle value on the gather axis. The fake
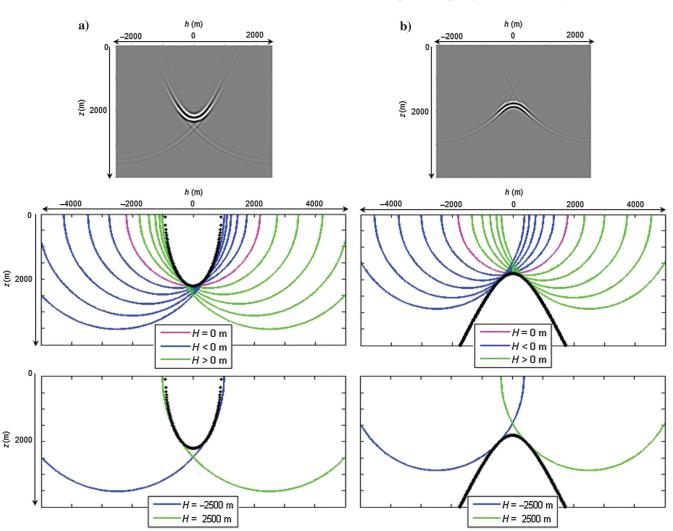

Figure 6. Imaging by the use of (a) 10% too-high and (b) 10% too-low migration velocity. The subsurface-offset CIGs are defocused, as shown on top. The accumulated extended impulse responses do not share a common intersection point with the vertical axis, as demonstrated by the illustrations.

dip-angle contribution of the kinematic artifacts was averaged out by the weight function.

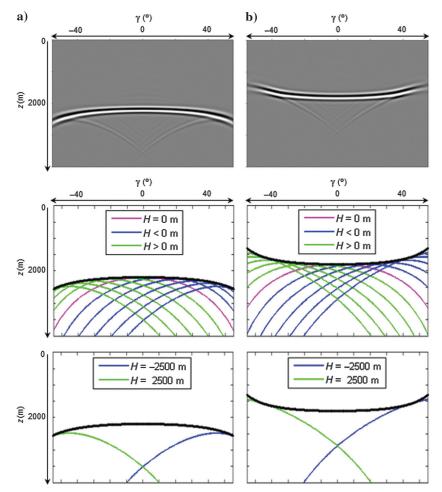## DIP-ANGLE DOMAIN SPECULARITY FILTER DESIGN

The prominent presence of the kinematic artifacts in the subsurface-offset domain and scattering-angle domain may impair the analysis of the extended image, especially when velocity errors are present. Almomin and Biondi (2014) address this problem in the context of tomographic FWI (TFWI). They derive a preconditioner for the acoustic wave equation that compensates for biased amplitude behavior of the reflection coefficient. Their preconditioned inversion algorithm significantly improves the convergence rate of TFWI by suppressing the kinematic artifacts.

In this study, we propose a different approach for this matter, based on a dip-angle criterion. Dip-angle information can be extracted from the prestack data to enhance the image quality and improve its reliability (Tabti et al., 2004; Qin et al., 2005; Bienati et al., 2009; Koren and Ravve, 2011; Dafni and Reshef, 2014). In relation to Kirchhoff migration, the stationary phase assumption implies that the Kirchhoff integral over the dip angles is constructive only along a limited dip aperture around the specular angle. The enhanced image is obtained by partial stacking of dip-angle ADCIGs, according

to the predefined specular dip model. Although wave-equation migrations lack the asymptotic imaging artifacts associated with Kirchhoff migrations, they do not result in noise-free images. The data truncation kinematic artifacts are just one example supporting this claim.

We use a dip-domain decomposition technique to first recognize the specular signal in the image, and then to reject any other signal that differs in dip from the specular direction. By "specular," we refer to a reflection trajectory that has its Snell's law normal coinciding with the normal to the subsurface reflector. The kinematic artifacts, as demonstrated in Figures 1 and 2, form a coherent but fake reflection image away from the zero-subsurface offset section. It is misplaced in depth, and dips with an angle that slightly differs from the specular angle (the larger the specular dip, the bigger the difference from the fake event's dip). However, as shown in Figure 3, the dip angle of the fake event is mainly determined by the acquisition configuration, and may vary in accordance. In the following, we exploit this nonspecular behavior of the kinematic artifacts along with their displacement in depth and subsurface offset to efficiently eliminate their contamination.

The extraction of a well-defined dip profile of the subsurface is enabled by recognizing the dominant spot-like events in the dip-angle ADCIGs. It is automated in this work in an adaptive manner by measuring the signal coherency in the dip-angle domain. We

Figure 7. Imaging in the scattering-angle domain by the use of (a) 10% too-high and (b) 10% too-low migration velocity. The scattering-angle ADCIGs show moveout curves, as shown on top. The envelope of the transformed accumulation of the extended impulse responses is curved, as demonstrated by the illustrations.

propose to exploit the subsurface-offset dependency of the dip-angle decomposition (i.e., the intermediate stage of the transform) for that measurement. It will turn out later in this paper to be crucial, when velocity errors are present. Therefore, the coherency is calculated in depth for each subsurface offset separately, via a conventional semblance coefficient S (Neidell and Taner, 1971), and with respect to the dip angle ν

$$S(z,\nu,h) = \frac{1}{2N_\nu + 1} \frac{\sum_{iz=z-N_z}^{z+N_z} \left(\sum_{i\nu=\nu-N_\nu}^{\nu+N_\nu} \mathrm{ADCIG}(iz,i\nu,h) \right)^2}{\sum_{iz=z-N_z}^{z+N_z} \sum_{i\nu=\nu-N_\nu}^{\nu+N_\nu} \mathrm{ADCIG}^2(iz,i\nu,h)}.$$

(9)

This is a local semblance formula, derived according to the depth half-window size N_z and the dip half-window size N_ν, for each dip angle in the gather. The choice for N_z and N_ν may vary from one data set to another. It reflects in some sense the Fresnel zone size and frequency bandwidth of the seismic data. The window size is predefined by the user, usually according to the size of a typical spot-like event in the dip-angle ADCIG. We use 25 m in depth and 6° in dip angle as the semblance half-window size in all synthetic examples presented in this paper. The semblance in equation 9

is designed to detect events that have less than a cycle of oscillation as a function of dip angle over the calculation window. The spot-like response of reflections in the dip domain has a horizontal phase orientation (i.e., the phase normal is vertical) regardless of how steep the reflector is dipping. It is dictated by the stationary phase of reflections at the specular dip. Figure 8a demonstrates that behavior by showing an event with more than a full oscillation, but it is entirely vertical. Therefore, the event is locally coherent with respect to the dip angles, and equation 9 is expected to yield a big-semblance score in accordance. However, the kinematic artifacts are also coherent in dip at nonzero-subsurface offsets, although they do not mark the specular dip and are misplaced in depth. Therefore, equation 9 is expected to pick some artificial but considerable semblance score that does not explain the specular reflections in the image.

At the top part of Figure 8b, three semblance profiles are displayed. They were calculated according to equation 9, and correspond to the subsurface-offset-dependent dip-angle ADCIGs shown at the top of Figure 8a. In the middle panel, the semblance maximizes at the place marking the center of the specular spot-like reflection. The two panels on the sides show the semblance imprint of the kinematic artifacts that marks a misleading dip-domain indication. To diminish the influence of the kinematic artifacts in our
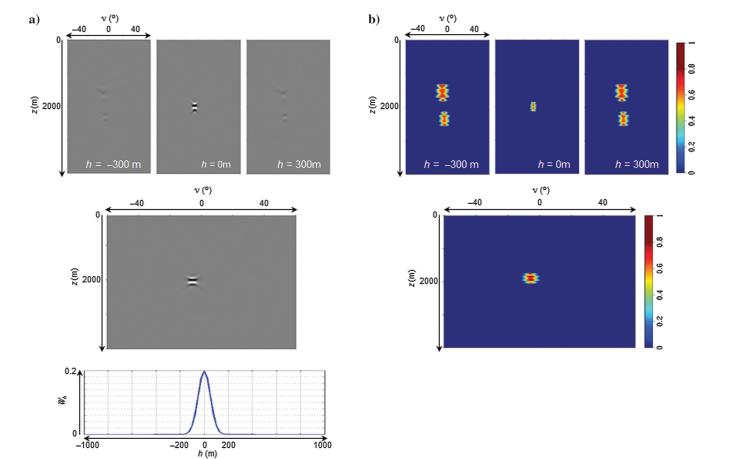

Figure 8. Transformation to the dip-angle domain. (a) Dip-angle ADCIG, computed at $x = 10,000$ m and (b) the corresponding specularity filter. First, the dip angles are decomposed for each subsurface offset individually (top), and then all subsurface offsets are averaged to form an effective dip-angle representation (bottom). This averaging is weighted by the Gaussian function at the bottom-left corner.

semblance analysis, we propose an additional averaging step that follows equation 9. Similar to the way, the dip-angle ADCIGs are derived, an averaging over all subsurface offsets is suggested

$$S_e(z, \nu) = \sum_h W_h S(z, \nu, h). \qquad (10)$$

It yields an effective coherency measure S_e, by weighting the intermediate semblance of all subsurface offsets according to the function W_h, proposed in equation 8. The effective semblance in equation 10 is expected to indicate about the true spot-like events only, while attenuating the misleading information of the kinematic artifacts. We use the same weight function, illustrated at the bottom of Figure 8a, to calculate the effective semblance in our example. It is presented at the bottom of Figure 8b and clearly shows an indication of the $-5°$ dipping reflector.

We propose a design for a dip-domain specularity filter in this study by using the effective semblance as weights to scale the dip-angle ADCIGs. The filter takes the form

$$F_{spec} = w \cdot S_e. \qquad (11)$$

The additional operator w is considered here as a shaping filter, modifying the original semblance profile. An entire spectrum of shaping options is available for w, according to the specularity content desired to be preserved in the image. It is demonstrated in this work by the following two end scenarios:

$$\begin{cases} w_{spec} = I, \\ w_{diff} = (S_e^{-1} - 1)I. \end{cases} \qquad (12)$$

The most intuitive application of F_{spec} is to enhance specular events in the gathers. It includes an identity matrix as the shaping operator w_{spec}. On the other hand, if diffraction imaging is our goal, the specular events would be suppressed by setting the shaping filter to w_{diff} (Koren and Ravve, 2011). The effective semblance at the bottom of Figure 8b exemplifies the first scenario in equation 12. It represents the specularity filter F_{spec}, obtained with the shaping of w_{spec}. Because the specularity filter highly correlates with the dip-angle ADCIG, its application as a weighting operator would enhance the specular event in the gather. Moreover, it is important to emphasize at this point that S_e and w are both normalized, which makes the specularity filter normalized as well. Therefore, the filter's application does not modify the amplitude's scale of the image.

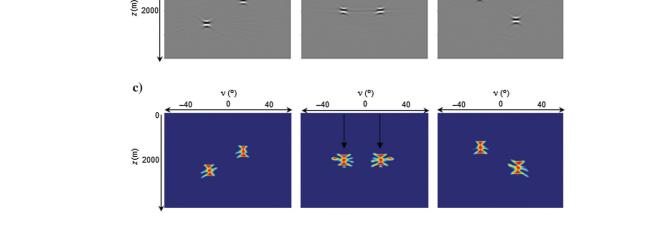Figure 9. Conflicting dips scenario. (a) The zero subsurface-offset image on the left to three subsurface-offset CIGs, (b) dip-angle ADCIGs, and (c) the corresponding specularity filter. The CIGs were calculated at the locations marked with the dashed lines.

The specularity filter is not necessarily singular in dip. It can recognize multiple events in the dip-angle domain based on their different dip quantity. We demonstrate this in Figure 9, in which a conflicting dips scenario is presented. The synthetic data for this example were acquired with the same acquisition geometry as in the previous example. For imaging, we used the correct migration velocity, and for the dip transform, we used the same narrow weight function W_h, plotted at the bottom of Figure 8a. The subsurface-offset extended image is shown in Figure 9a. The zero subsurface-offset section is displayed to the left of three subsurface-offset CIGs. These CIGs were calculated at the locations marked with the dashed black lines. The middle gather represents the conflicting dips situation, where the two focused reflections perfectly overlap. The dip-angle ADCIGs in Figure 9b show two separated spot-like events that indicate a 15° and −20° dipping reflections (marked with the black arrows). In the dip domain, we clearly distinguish between the two events, even at the conflicting location (i.e., the middle gather). The specularity filter is constructed in Figure 9c with the shaping operator w_{spec}. The filter yields two evident marks centered at the specular dip angle values (i.e., 15° and −20°) and correlates with the dip-angle ADCIGs.

SPECULARITY FILTER APPLICATION

The workflow involving the application of the specularity filter is illustrated in Figure 10. First, the seismic data are migrated by a subsurface-offset extended wave-equation PSDM operator. Then, the intermediate subsurface-offset-dependent dip-angle ADCIGs are computed. The coherency of the migrated signal in the dip domain is measured next by the semblance formula for each subsurface offset (equation 9), and then averaged to produce the effective semblance (equation 10). The specularity filter is constructed accordingly, by applying the shaping operator (equation 11). In the following stage, the filter is applied as a dip-angle weighting function, in which each subsurface-offset-dependent dip-angle ADCIGs is scaled individually. Finally, the last step includes an inverse transformation of the filtered gathers from the dip domain back to the subsurface-offset domain for further noise-free analysis. Two low-clip operations are also included in the workflow, only for the purpose of constructing the specularity filter: energy and semblance clip. The first clips to zero any energy (amplitude square) below a given threshold in the subsurface-offset-dependent dip-angle ADCIGs. This clipping is essential because the semblance calculation is highly sensitive to outliers. The second clips low semblance values to make the effective semblance

profile more smooth and reliable. In the examples provided in this study, we use no more than 1% energy clip, and no more than 20% semblance clip.

The application of the proposed filter is illustrated in the following two synthetic examples: First, we demonstrate the elimination of the data truncation kinematic artifacts discussed earlier in this paper. The elimination is shown as highly effective also in the case
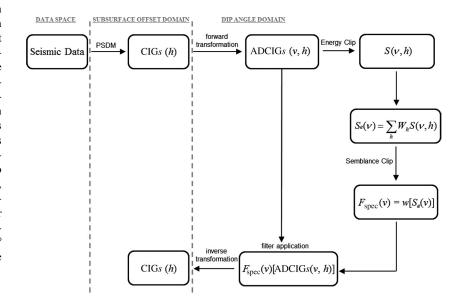

Figure 10. The specularity filter application's workflow. The seismic data are migrated first by a subsurface-offset extended imaging operator. Then, it is transformed to the dip-angle domain, in which the specularity filter is constructed and applied. Finally, the image is inverse transformed back to the subsurface-offset domain.
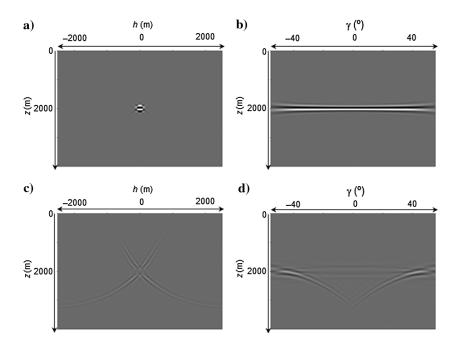

Figure 11. The application of the specularity filter. The specular reflection is enhanced in (a) the subsurface-offset domain and (b) the scattering-angle domain. The specular reflection is suppressed in (c) the subsurface-offset domain and (d) the scattering-angle domain.

in which erroneous migration velocity is used. Then, the specularity filter is applied to suppress random and coherent noise, inserted artificially to the extended image.

Kinematic artifacts elimination

The mechanism responsible for the kinematic artifacts, observed in the subsurface-offset domain, is linked to the truncation of the data acquisition geometry. These artifacts can be suppressed in the data space by tapering the long acquisition offset traces, but with limited success and by impairing the recorded data's true amplitude scaling. The dip-domain specularity filter is an alternative applied in the image space for the same task. Because the appearance of the artifacts has nothing to do with the structural settings of the model, they are filtered by a simple dip-domain criterion. The elimination process is demonstrated next by the $-5°$ dipping reflector example described above. The corresponding subsurface-offset CIG and dip-angle ADCIG have already been shown in Figures 1b and 8a, along with the specularity filter in Figure 8b. What is left according to the diagram in Figure 10 is to apply the filter on the subsurface-offset-dependent dip-angle ADCIG and inverse transform back to the subsurface-offset domain. Figure 11a shows the resulting subsurface-offset CIG. There is no evidence whatsoever for the contamination of the kinematic artifacts. The noise-free image is perfectly focused at zero subsurface offset. Moreover, the scattering-angle ADCIG is now computed in Figure 11b and shows only the expected flat event at the true depth of reflection. No remnant imprint is left to indicate about the two hyperbolic diffraction curves that were recognized originally at the maximum angle of illumination in Figure 5.

One of the most remarkable features of the specularity filter is its ability to suppress or enhance different parts of the specularity content. This is achieved by the shaping filter w in the construction of the filter. By using w_{diff} as the shaping filter (see equation 12), the strong and coherent specular content is suppressed and other events,

which do not have a well-defined specular dip, are untouched. These might include noise or artifacts, but it can also include structural features causing seismic diffractions. Thus, we consider w_{diff} as a filter designed for diffraction imaging. The application of this filter is demonstrated in Figure 11c and 11d. In the subsurface-offset domain (Figure 11c), the focused event at zero offset is eliminated, and the kinematic artifacts are clearly preserved. Furthermore, the decomposition of the scattering-angle ADCIG (Figure 11d) yields only the hyperbolic curves on both sides of the excluded flat event.

Erroneous migration velocity impairs the focusing or the flatness of the prestack image (subsurface-offset or scattering-angle domain, respectively). However, the formation of the kinematic artifacts is as prominent as in the true velocity case. The application of the specularity filter in relation to the wrongly migrated images, shown in Figures 6 and 7, successfully suppresses the artifacts without harming the defocusing or moveout information. This is essentially achieved by the subsurface-offset dependency of the specularity filter construction, in which each offset is analyzed separately in the dip domain before all offsets are averaged by the weight function W_h. Because velocity errors defocus the image away from the zero subsurface offset, we used here a relatively wide variance for W_h ($\sigma = 300$ m), to maintain the defocusing information. The corresponding filters for the 10% too-high and too-low velocities are presented at the top and bottom of Figure 12a, respectively. Although the specular spot is slightly smeared and misplaced in depth, it was still found efficient with regard to the artifacts' removal. The resulting filtered subsurface-offset CIGs and scattering-angle ADCIGs are presented in Figure 12b and 12c, respectively. We expect these artifact-free gathers to result in faster and more accurate inversion of medium parameters. In particular, we see a great potential in combining the specularity filter with migration operators derived asymptotically as the approximate inverse (rather than adjoint) of the Born scattering operator, such as the one proposed by Hou and Symes (2015). Although these approximate inverse operators
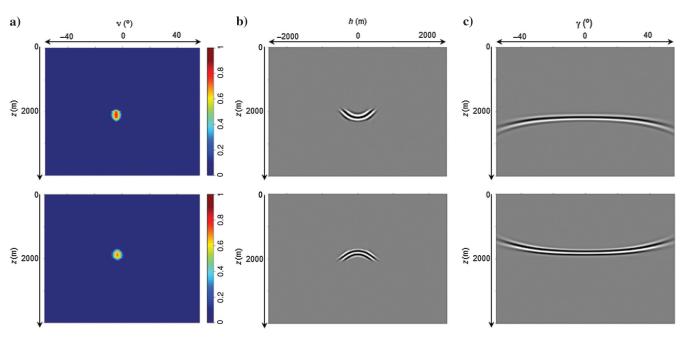

Figure 12. The application of the specularity filter in relation to 10% too-high and 10% too-low migration velocity (top and bottom parts, respectively). (a) The specularity filter, (b) the filtered subsurface-offset CIGs, and (c) the filtered scattering-angle ADCIGs.

result in an image that usually better explains the seismic data, they are still impaired by the kinematic artifacts. The involvement of the specularity filter to diminish these artifacts would assist to fit the data even better and faster with the approximate inverse.

Noise elimination

Seismic imaging methods applied to field data sets are often affected by noise, mainly due to the gap differentiating theory from practice. In the following synthetic example, random and coherent noises were artificially added to the extended image. The random noise was set to peak around the zero subsurface-offset trace, in which the true reflection events focus. The coherent noise was inserted as a fake reflection event, focused coherently at a nonphysical subsurface offset ($h = -500$ m in this example). Therefore, it is coherent in the -500 m subsurface-offset section of the extended image, and dips with a $-5°$ dip angle. The application of the

specularity filter is tested here to suppress these two types of noise. Any feature in the image space that does not have a well-defined physical dip direction is expected to be successfully eliminated by the action of the filter.

Our example includes a model of four curved subsurface reflectors and a perfectly known velocity model. The same acquisition geometry and source wavelet as in the previous example were used to generate the synthetic data. The extended image was calculated by the migration operator in equation 1, before the artificial noise was added. The noisy zero subsurface-offset image is provided in Figure 13a. The dashed black lines mark the locations, where CIGs are displayed in this example. Figure 14a presents the noisy set of subsurface-offset CIGs above the corresponding set of scattering-angle ADCIGs. The four seismic events are identified in the gathers behind the randomly spread noise. Because the fake reflection event was forced to focus away from the zero subsurface offset, it is absent from the image in Figure 13a. However, it is present coherently
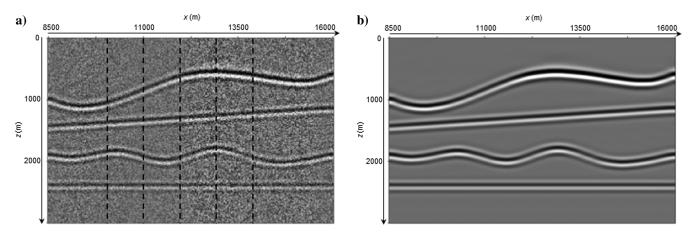

Figure 13. Imaging of a four subsurface reflector model. (a) The noise contaminated zero-subsurface offset image and (b) the filtered zero-subsurface offset image.
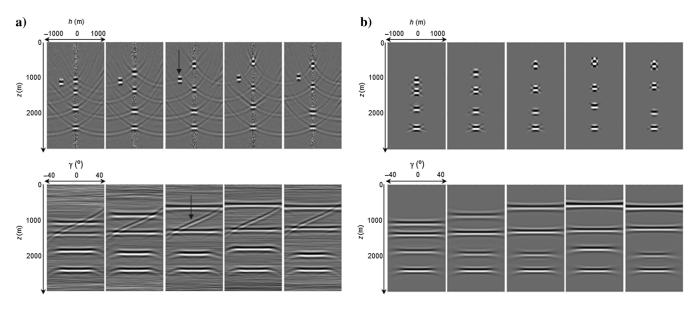

Figure 14. A set of subsurface-offset CIGs above the corresponding set of scattering-angle ADCIGs (a) before and (b) after the application of the specularity filter.

in the gathers in Figure 14a (marked with the black arrows). It is recognized as an inclined event, rather than flat, after the angle transformation at the bottom of Figure 14a. In real life, this might enforce additional (but obviously not required) velocity optimization steps, by considering this event as true.
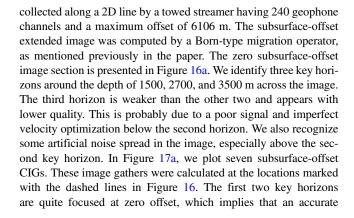
Dip-angle ADCIGs were calculated as well for the construction of the specularity filter. In Figure 15a, we present the final dip gathers, after averaging the subsurface offsets by W_h. Because there are no velocity errors in this example, we used the same narrow weight function for this averaging as shown at the bottom of Figure 8a. Four well-focused specular spots are clearly recognized in the dip domain, indicating the local dip direction of the subsurface reflectors. The random noise is still present in the gathers but without a clear dip direction. Therefore, it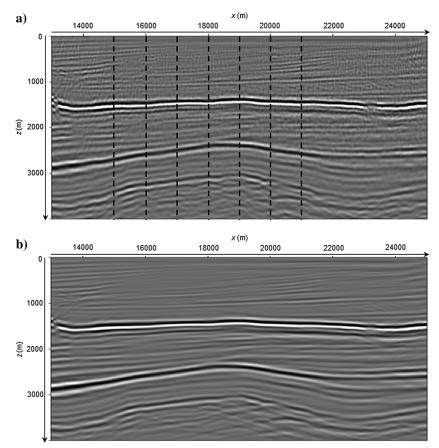 is expected to be removed by the following application of the filter. The fake reflection event of this example (i.e., the coherent noise) is absent from the gathers in Figure 15a. Although it should indicate a $-5°$ dipping event, it was eliminated with the averaging by W_h.
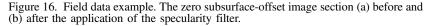
Because specular enhancement is our goal in this example, w_{spec} was chosen according to equation 12 as the shaping filter involved in the workflow. The resulting specularity filter, calculated at the same locations as the other gathers, is displayed in Figure 15b. The resemblance with the specular spots of the dip-angle ADCIGs is prominent. Finally, the specular filter was applied in the dip domain for each subsurface offset individually, before the gathers were inverse transformed back to the subsurface-offset domain. The filtered zero subsurface-offset image is shown in Figure 13b, along with the subsurface-offset CIGs at the top of Figure 14b. The random noise is significantly suppressed in the image, the kinematic artifacts are removed, and no evidence remains for the fake event. For further analysis of the filtered image, scattering-angle ADCIGs are computed at the bottom of Figure 14b. Comparing these gathers with the original set in Figure 14a emphasizes the comprehensive job done by the specularity filter.

FIELD DATA EXAMPLE

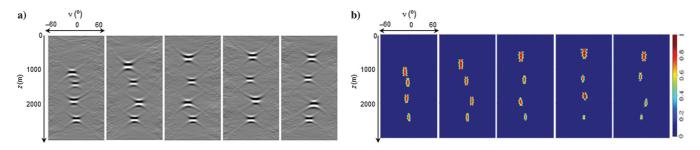We demonstrate next our specularity filter application on a field data set acquired offshore in the east Mediterranean Sea. The data were collected along a 2D line by a towed streamer having 240 geophone channels and a maximum offset of 6106 m. The subsurface-offset extended image was computed by a Born-type migration operator, as mentioned previously in the paper. The zero subsurface-offset image section is presented in Figure 16a. We identify three key horizons around the depth of 1500, 2700, and 3500 m across the image. The third horizon is weaker than the other two and appears with lower quality. This is probably due to a poor signal and imperfect velocity optimization below the second horizon. We also recognize some artificial noise spread in the image, especially above the second key horizon. In Figure 17a, we plot seven subsurface-offset CIGs. These image gathers were calculated at the locations marked with the dashed lines in Figure 16. The first two key horizons are quite focused at zero offset, which implies that an accurate

Figure 16. Field data example. The zero subsurface-offset image section (a) before and (b) after the application of the specularity filter.

Figure 15. A set of (a) dip-angle ADCIGs are computed to construct the (b) specularity filter in the dip domain.
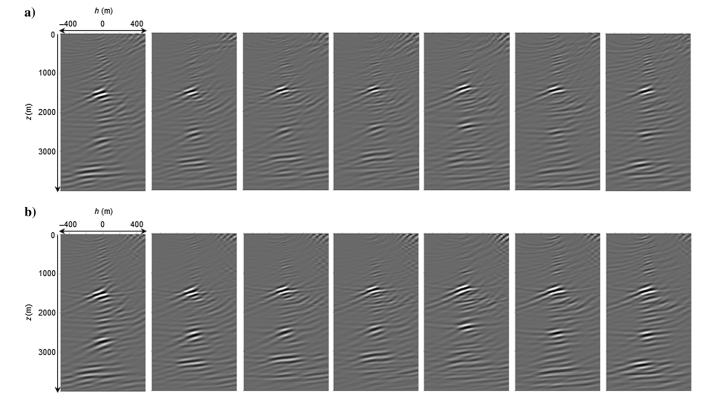
a)

b)

Figure 17. Field data example. Subsurface-offset CIGs (a) before and (b) after the application of the specularity filter.
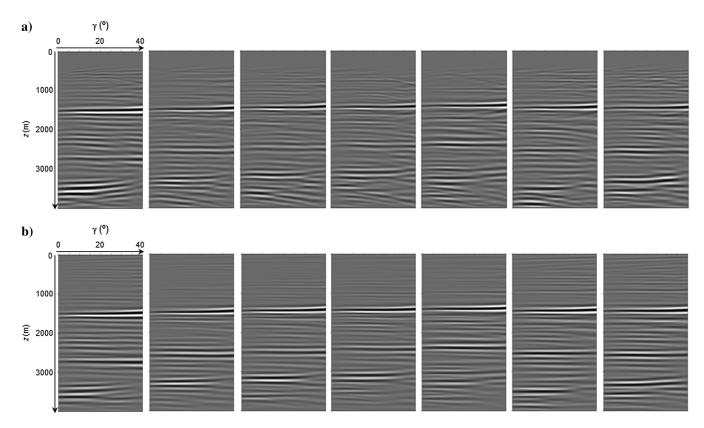
a)

b)

Figure 18. Field data example. Scattering-angle ADCIGs (a) before and (b) after the application of the specularity filter.

migration velocity was used. The third horizon is slightly defocused due to the nonoptimized velocity at this depth.

Scattering-angle ADCIGs were computed by Radon transforming the subsurface-offset extended image. We present seven of them in Figure 18a, for the same marked horizontal locations. Note that because a single-ended spread was used to acquire the data (all geophones towed behind the seismic source), only positive scattering angles were decomposed. As expected, the first two key horizons are fairly flat in the gathers, whereas the third horizon has poor quality and shows some remnant moveout. Extracting residual moveout from the deep part of the gathers for further velocity optimization might become a challenge. The poor signal and artifacts at this depth make the picking task ambiguous and inconclusive.

We also generated dip-angle ADCIGs for the specularity filter operation and they are shown in Figure 19a. We used the weight function W_h with a variance of $\sigma = 100$ m to average all subsurface offsets in the dip transform. Spot-like events are clearly identified in the dip gathers. Their position on the angle axis indicates the local specular dip direction of the subsurface structure. Notice that away from these spots, some nonspecular noise is contaminating the gathers. The application of the specularity filter in this example is goal-oriented to eliminate this type of noise. Therefore, we chose w_{spec} out of equation 12 as the shaping filter involved in the filter design. The resulting specularity filter, calculated at the same locations as the other gathers, is displayed in Figure 19b. The filter is highly correlated with the specular spots in the dip-angle ADCIGs.

We applied the specularity filter in the dip domain for each subsurface offset individually, and transformed the image back to the subsurface-offset domain. The filtered zero-subsurface offset image section is shown in Figure 16b. A comparison with the original

image section shown above in this figure indicates that the noise spread across the image was successfully suppressed, while keeping the continuity of the prominent key horizons. The filtered subsurface-offset CIGs are plotted in Figure 17b. In the gather domain, we notice that the focused-in-offset events were enhanced. They appear in the gathers with stronger amplitude, especially in the deeper part. We retransformed the filtered image to the scattering-angle domain for further analysis. The filtered scattering-angle ADCIGs are displayed in Figure 18b. The enhancement of the events and the noise suppression are even more substantial in the angle domain. The key horizons are now more distinguished in the gathers. The increase in quality of the ADCIGs alleviates some of the difficulties involved with picking residual moveout below the second key horizon. The supervised application of the specularity filter did not impair this moveout information but made it more prominent for analysis. An accurate angle-domain moveout picking is of course essential for the improvement of the velocity function optimization at the deep part of the model.

CONCLUSIONS

Postmigration analysis of ADCIGs in the dip-angle domain is not restricted solely to Kirchhoff migration. It can also be derived from wave-equation migration methods, extended by the subsurface offset. Dip-angle information, extracted from dip-angle ADCIGs, is directly related to the subsurface structure and distinguishes specular reflections from coherent or incoherent noise. Incorporating this information into the conventional migration velocity and amplitude analysis is essential for their success. Our methodology characterizes specular reflections as spot-like events in the dip-angle domain,
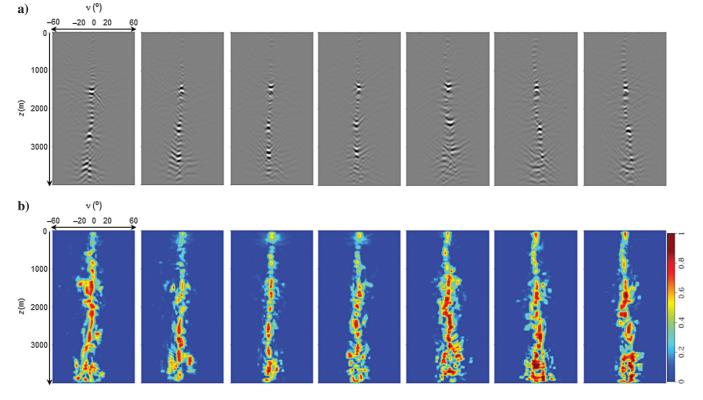

Figure 19. Field data example. (a) Dip-angle ADCIGs are computed to construct the (b) specularity filter in the dip domain.

indicating the local dip in the subsurface. A specularity filter was designed in the dip domain to pass only energy related to specular reflection events. Other similar filters may be designed to enhance (or eliminate) different types of events in the CIGs, distinguished by their specularity character in the dip domain.

The workflow involving the application of the specularity filter takes place in the image space. It is based on invertible Radon transformation of the subsurface-offset extended image to the dip-angle domain. Therefore, no remigration of the seismic data is required. The extended image is transformed to the dip-angle domain in which the specularity filter is applied, and then inverse transformed back for further analysis of the filtered subsurface-offset CIGs. Moreover, by an additional transformation to the scattering-angle domain, the analysis of the conventional angle-dependent reflection coefficient is enhanced. A key element of the proposed filter is the exploitation of the subsurface-offset extension. The dip-domain transform is suggested not only for the image at zero subsurface offset but for the entire range of offsets. The dip-angle information of each offset is weighted as a function of its distance from the zero offset and with respect to the reliability of the migration velocity. This supports the defocusing information of the image due to velocity errors, and assists to maintain it while applying the filter.

The specularity filter was applied successfully to eliminate random and coherent noise inserted artificially to synthetic data sets. Furthermore, it succeeded in improving the image quality of a field data set, by enhancing the response of the key reflection events in the filtered CIGs. However, the filter is not expected to be as efficient when coherent noise that dips with the specular dip angle contaminates the image at zero-subsurface offset (such as surface multiples).

We also addressed the issue involving the appearance of kinematic artifacts in the extended subsurface-offset image volume. These artifacts commonly emerge as an edge effect related to the seismic survey design. It is a consequence of an abrupt truncation of the acquisition geometry by the edges of the survey extent. A formation mechanism was suggested for these artifacts by considering the seismic migration as a superposition of subsurface-offset extended impulse responses, contributed by individual data traces. The response of those data traces, acquired at the acquisition geometry's boundary, is accumulated in the image space with an incomplete destructive interference, forming the mentioned kinematic artifacts. Under the assumption of a homogeneous medium, the signature of these artifacts in the subsurface-offset CIGs is elliptic. It is characterized by the acquisition offset of the data traces at the acquisition's boundary. The elliptic artifacts are transformed into hyperbolic-shaped artifacts, once scattering-angle ADCIGs are decomposed. The hyperbolic signature in the scattering-angle domain is also a function of the corresponding acquisition offset, and it has its apex at the maximum angle of illumination. The same mechanism was suggested for the kinematic artifacts emergence in the case when erroneous migration velocity is used. A similar elliptic/hyperbolic signature has been revealed in the CIGs, by taking into account the relative velocity error. Because the kinematic artifacts are obviously not related to the subsurface geology, their elimination by the specularity filter is highly effective. The ability to remove these artifacts without harming the significant defocusing or moveout information provided by the CIGs is expected to essentially improve the accuracy of the postmigration analysis, and accelerate the convergence of inversion methods for the medium parameters. Furthermore, the specularity filter is expected to annihilate any type of artifact in the image space by its unique dip-domain criterion, as long as the formation mechanism of the artifact is nonspecular.

Shaping the specularity filter appropriately to enhance small-scale structural features related to seismic diffractions was discussed briefly in this paper. Seismic diffractions are distinguished from reflections by their unique dip-angle response. Their recognition and enhancement in the seismic image, based on the specularity filter application, might reveal valuable and high-resolution information about the subsurface-medium properties. We believe that diffraction imaging established on wave-equation migration methods, such as the one implied in this study, is quite promising and might have a great impact in improving our understanding of the interior of the earth.

The extension of the proposed specularity filter to 3D may follow the same dip-angle construction, although the dip direction in a 3D space is composed by a system of two angles, consisting of the dip and the dip-azimuth. Reflections are expected to have a similar spot-like signature in the polar 3D dip-angle system at the specular dip and dip-azimuth location. However, dip-angle decomposition in 3D space requires further study, and it is out of the scope of this paper.

ACKNOWLEDGMENTS

APPENDIX A

PARAMETRIC RADON TRANSFORMATION

In this appendix, we formulate a parametric representation for the Radon transform operator. It is used to transform the subsurface-offset extended impulse response to the scattering-angle domain. We derive a hyperbolic expression, which we use in this paper to explain the accumulative construction of the image in the angle domain.

The extended impulse response, as introduced in equation 4, has an elliptic appearance in the subsurface-offset domain:

$$\frac{(h - H)^2}{\varepsilon^2(z_0^2 + H^2)} + \frac{z^2}{\varepsilon^2(z_0^2 + H^2) - \Delta x^2} = 1. \qquad \text{(A-1)}$$

This ellipse is represented in a parametric form as

$$z = \cos\theta\sqrt{\varepsilon^2(z_0^2 + H^2) - \Delta x^2},$$
$$h = H + \sin\theta\sqrt{\varepsilon^2(z_0^2 + H^2)}. \qquad \text{(A-2)}$$

The auxiliary angle θ ranges from 0 to 2π radians. It defines a point on the two circles having their radius as the semiminor and semimajor axes of the ellipse, and centered at $(H, 0)$.

Our angle decomposition techniques transform the subsurface-offset extended image to the angle domain by Radon transform operators. The transformation to the scattering-angle domain may be cast as a parametric Radon transform as follows:

$$z(p) = z + ph, \tag{A-3}$$

where $p = \tan \gamma$ is the transform's slope and γ stands for the scattering angle. Here, $z(p)$ is the imaging depth in the scattering-angle domain. An expression for the slope p is derived from its definition and with respect to the ellipse in equation A-1:

$$p = -\frac{\partial z}{\partial h} = \frac{1}{\eta^2}\frac{(h - H)}{z}, \tag{A-4}$$

where η is considered here as a stretch factor, expressing the ratio between the semimajor and semiminor axes of the ellipse:

$$\eta = \sqrt{\frac{\varepsilon^2(z_0^2 + H^2)}{\varepsilon^2(z_0^2 + H^2) - \Delta x^2}}. \tag{A-5}$$

According to the parametric representation of the ellipse in equation A-2, we rewrite the right side of equation A-4 as

$$p = -\frac{\partial z}{\partial h} = \frac{1}{\eta}\tan \theta. \tag{A-6}$$

Note that equation A-6 shows the relations between the scattering-angle γ and the auxiliary angle θ, according to the stretch factor η. In the special case where a zero-dip reflector is imaged, the imaging aperture goes to zero ($\Delta x = 0$), and therefore the stretch factor vanishes ($\eta = 1$). In such cases, the two angles are equal: $\gamma = \theta$.

We use the relation in equation A-6 to change variables in equation A-2, and express the subsurface-offset domain ellipse with respect to the scattering angle γ. It yields the following representation:

$$z = \frac{1}{\sqrt{1 + p^2\eta^2}}\sqrt{\varepsilon^2(z_0^2 + H^2) - \Delta x^2},$$
$$h = H + \frac{p\eta}{\sqrt{1 + p^2\eta^2}}\sqrt{\varepsilon^2(z_0^2 + H^2)}. \tag{A-7}$$

Substitution of equation A-7 into equation A-3 gives

$$z(p) = \frac{1}{\sqrt{1 + p^2\eta^2}}\sqrt{\varepsilon^2(z_0^2 + H^2) - \Delta x^2} + pH$$
$$+ \frac{p^2\eta}{\sqrt{1 + p^2\eta^2}}\sqrt{\varepsilon^2(z_0^2 + H^2)}. \tag{A-8}$$

Finally, we rearrange the terms in equation A-8 to obtain

$$z(p) = \sqrt{(\varepsilon^2(z_0^2 + H^2) - \Delta x^2)(1 + p^2\eta^2)} + pH. \tag{A-9}$$

Equation A-9 is a hyperbolic equation. It represents the image response of a single data trace in the scattering-angle domain. Hence, it is considered as the angle-domain variant of the extended impulse

response. The Radon transformation to the angle domain turns the elliptic responses into hyperbolas. The superposition of all the hyperbolas constructs an envelope of the angle-domain image.

The only assumption made through the formulation of equation A-9 was about the homogeneity of the subsurface. Therefore, it describes the general case of having an unknown (but constant) migration velocity and a single seismogram recorded on the surface. In this paper, we use equation A-9 to study the angle-domain image of dipping reflections. However, it may also be useful to describe seismic diffractions in the angle domain.

REFERENCES

Almomin, A., and B. Biondi, 2014, Preconditioned tomographic full waveform inversion by wavelength continuation: 84th Annual International Meeting, SEG, Expanded Abstracts, 944–948.

Audebert, F., L. Nicoletis, P. Froidevaux, and H. Rakotoarisoa, 2003, True amplitude migration in the angle domain by regularization of illumination: 73rd Annual International Meeting, SEG, Expanded Abstracts, 921–924.

Baina, R., S. Nguyen, N. Noble, and G. Lambare, 2003, Optimal anti-aliasing for ray-based Kirchhoff depth migration: 73rd Annual International Meeting, SEG, Expanded Abstracts, 1130–1133.

Baina, R., E. Zamboni, and G. Lambare, 2006, How to cope with smoothing effect in ray based PSDM?: 68th Annual International Conference and Exhibition, EAGE, Extended Abstracts, G045.

Bartana, A., D. Kosloff, and I. Ravve, 2006, Discussion and reply on "Angle-domain common-image gathers by wavefield continuation methods" (Paul C. Sava and Sergey Fomel, 2003, Geophysics, 68, 1065–1074): Geophysics, **71**, no. 1, X1–X3, doi: 10.1190/1.2168013.

Bienati, N., C. Andreoletti, F. Perrone, V. Lipari, and M. Giboli, 2009, Limited aperture migration in the angle domain: 71st Annual International Conference and Exhibition, EAGE, Extended Abstracts, U005.

Bleistein, N., 1987, On the imaging of reflectors in the earth: Geophysics, **52**, 931–942, doi: 10.1190/1.1442361.

Červený, V., 2001, Seismic ray theory: Cambridge University Press.

Chen, J., 2004, Specular ray parameter extraction and stationary-phase migration: Geophysics, **69**, 249–256, doi: 10.1190/1.1649392.

Claerbout, J. F., 1985, Imaging the earth's interior: Blackwell Scientific Publishing.

Dafni, R., and M. Reshef, 2014, Image enhancement by multi-parameter characterization of common image gathers: Geophysical Prospecting, **62**, 1453–1467, doi: 10.1111/1365-2478.12155.

Dafni, R., and W. W. Symes, 2016, Scattering and dip angle decomposition based on subsurface offset extended wave-equation migration: Geophysics, **81**, no. 3, S119–S138, doi: 10.1190/geo2015-0528.1.

Fomel, S., E. Landa, and M. T. Taner, 2007, Poststack velocity analysis by separation and imaging of seismic diffractions: Geophysics, **72**, no. 6, U89–U94, doi: 10.1190/1.2781533.

Gray, S. H., J. Etgen, J. Dellinger, and D. Whitmore, 2001, Seismic migration problems and solutions: Geophysics, **66**, 1622–1640, doi: 10.1190/1.1487107.

Hou, J., and W. W. Symes, 2015, An approximate inverse to the extended Born modeling operator: Geophysics, **80**, no. 6, R331–R349, doi: 10.1190/geo2014-0592.1.

Khaidukov, V., E. Landa, and T. J. Moser, 2004, Diffraction imaging by focusing-defocusing: An outlook on seismic super resolution: Geophysics, **69**, 1478–1490, doi: 10.1190/1.1836821.

Klokov, A., and S. Fomel, 2012, Separation and imaging of seismic diffractions using migrated dip-angle gathers: Geophysics, **77**, no. 6, S131–S143, doi: 10.1190/geo2012-0017.1.

Koren, Z., and I. Ravve, 2010, Specular/diffraction imaging by full azimuth subsurface angle domain decomposition: 80th Annual International Meeting, SEG, Expanded Abstracts, 3268–3272.

Koren, Z., and I. Ravve, 2011, Full-azimuth subsurface angle domain wavefield decomposition and imaging. Part I: Directional and reflection image gathers: Geophysics, **76**, no. 1, S1–S13, doi: 10.1190/1.3511352.

Landa, E., S. Fomel, and M. Reshef, 2008, Separation, imaging and velocity analysis of seismic diffractions using migrated dip-angle gathers: 78th Annual International Meeting, SEG, Expanded Abstracts, 2176–2180.

Landa, E., and S. Keydar, 1998, Seismic monitoring of diffraction images for detection of local heterogeneities: Geophysics, **63**, 1093–1100, doi: 10.1190/1.1444387.

Miller, D., M. Oristaglio, and G. Beylkin, 1987, A new slant on seismic imaging: Migration and integral geometry: Geophysics, **52**, 943–964, doi: 10.1190/1.1442364.

Moser, T. J., 2011, Non-smooth Kirchhoff migration: 81st Annual International Meeting, SEG, Expanded Abstracts, 3346–3350.

Mulder, W. A., 2014, Subsurface offset behaviour in velocity analysis with extended reflectivity images: Geophysical Prospecting, **62**, 17–33, doi: 10.1111/1365-2478.12073.

Neidell, N. S., and M.T. Taner, 1971, Semblance and other coherency measures for multichannel data: Geophysics, **36**, 482–497, doi: 10.1190/1.1440186.

Prucha, M., B. Biondi, and W. W. Symes, 1999, Angle-domain common-image gathers by wave-equation migration: 69th Annual International Meeting, SEG, Expanded Abstracts, 824–827.

Qin, F., B. Wang, P. Zhang, and F. Audebert, 2005, Kirchhoff preSDM interactive dip-gather stacking and dip illumination panel generation: 75th Annual International Meeting, SEG, Expanded Abstracts, 1882–1885.

Ravve, I., and Z. Koren, 2011, Full-azimuth subsurface angle domain wavefield decomposition and imaging. Part 2: Local angle domain: Geophysics, **76**, no. 2, S51–S64, doi: 10.1190/1.3549742.

Reshef, M., and E. Landa, 2009, Post-stack velocity analysis in the dip-angle domain using diffractions: Geophysical Prospecting, **57**, 811–821, doi: 10.1111/j.1365-2478.2008.00773.x.

Reshef, M., N. Lipzer, R. Dafni, and E. Landa, 2011, 3D post-stack interval velocity analysis with effective use of datuming: Geophysical Prospecting, **60**, 18–28, doi: 10.1111/j.1365-2478.2011.00962.x.

Stolk, C. C., M. V. de Hoop, and W. W. Symes, 2009, Kinematics of shot-geophone migration: Geophysics, **74**, no. 6, WCA19–WCA34, doi: 10.1190/1.3256285.

Symes, W. W., 2008, Migration velocity analysis and waveform inversion: Geophysical Prospecting, **56**, 765–790, doi: 10.1111/j.1365-2478.2008.00698.x.

Tabti, H., L. Gelius, and T. Hellmann, 2004, Fresnel aperture prestack depth migration: First Break, **22**, 39–46, doi: 10.3997/1365-2397.2004005.

ten Kroode, F., 2012, A wave-equation-based Kirchhoff operator: Inverse Problems, **28**, 115013, doi: 10.1088/0266-5611/28/11/115013.

Trorey, A. W., 1970, A simple theory for seismic diffractions: Geophysics, **35**, 762–784, doi: 10.1190/1.1440129.

Xu, S., H. Chauris, G. Lambare, and M. S. Noble, 2001, Common-angle migration: A strategy for imaging complex media: Geophysics, **66**, 1877–1894, doi: 10.1190/1.1487131.